nature climate change

Article

https://doi.org/10.1038/s41558-026-02559-3

# ENSO shapes salinity regimes and fish migration in the China Seas

Received: 11 June 2025

Accepted: 9 January 2026

Published online: 13 February 2026

Check for updates

Zhixuan Wang[1,2,10], Han Huang[3,10], Guizhi Wang[1,4,11] ✉, Tangdong Qu[5], Yue Liu[1], Xianghui Guo[1], Shiyun Lei[6], Jianyu Hu[1], Jingfang Fan[3,7], Jianping Gan[2], Ling Cao[1], Xiaosong Chen[3,8] & Minhan Dai[1,9,11] ✉

Salinity shapes ocean circulation and marine biogeography, yet its long-term spatiotemporal variability and ecological impacts in marginal seas remain poorly constrained. We reconstruct a high-resolution sea surface salinity dataset (2000–2020) for the China Seas using a machine learning framework that integrates in situ cruises and buoys with satellite observations and diagnose drivers with an eigen microstates approach. The El Niño/Southern Oscillation (ENSO) is the dominant control, modulating evaporation–precipitation, river discharge and Kuroshio intrusion. During El Niño, sea surface salinity increases by up to 25% in ocean-dominated regions but decreases up to 21% in river-dominated zones, amplifying meridional salinity contrasts. Species-distribution models indicate a southward habitat shift up to 2.5° latitude for 90% of key fish species. Under projected ENSO intensification, salinity inhomogeneity and associated ecological impacts are likely to strengthen. These results support an 'ENSO forcing–salinity–fishery' positive feedback framework and call for integrating salinity dynamics into adaptive, climate-informed fisheries management.

Under accelerating global climate change and subsequent intensification of the water cycle, the salinity of the ocean and its spatial patterns have undergone increasingly pronounced alterations over the past decades[1–3]. Spatially coherent multidecadal increasing (decreasing) trends have been reported in evaporation (precipitation)-dominated regions, described as the Clausius–Clapeyron expectation: "salty get saltier, fresh get fresher"[4–7]. This pattern has been attributed to various drivers, including river discharge, precipitation, evaporation, ice melt and large-scale climate modes such as El Niño/Southern Oscillation (ENSO)[2]. Salinity changes can affect the survival, growth and distribution of marine organisms[8,9] by disrupting the osmoregulatory balance, potentially causing physiological stress or even mortality[10,11], especially during strong El Niño and La Niña[12–14]. Revealing long-term spatiotemporal variations and underlying mechanisms of ocean salinity remains a central focus in climatic and marine ecosystem research and yet a daunting challenge, largely due to limited observational data.

This challenge is especially pronounced in ocean margins, such as the China Seas, where complex ocean dynamics and multiscale processes hinder reliable long-term observations[15,16]. The China Seas, encompassing the Bohai Sea, the Yellow Sea, the East China

[1]State Key Laboratory of Marine Environmental Science & College of Ocean and Earth Sciences, Xiamen University, Xiamen, China. [2]Department of Ocean Science and Department of Mathematics, Hong Kong University of Science and Technology, Hong Kong, China. [3]School of Systems Science / Institute of Nonequilibrium Systems, Beijing Normal University, Beijing, China. [4]Fujian Provincial Key Laboratory for Coastal Ecology and Environmental Studies, Xiamen University, Xiamen, China. [5]Joint Institute for Regional Earth System Science and Engineering, University of California, Los Angeles, CA, USA. [6]Carbon Neutral Innovation Research Center, Xiamen University, Xiamen, China. [7]Potsdam Institute for Climate Impact Research, Potsdam, Germany. [8]Institute for Advanced Study in Physics and School of Physics, Zhejiang University, Hangzhou, China. [9]Fujian Ocean Innovation Center, Xiamen, China. [10]These authors contributed equally: Zhixuan Wang, Han Huang. [11]These authors jointly supervised this work: Guizhi Wang, Minhan Dai. ✉e-mail: gzhwang@xmu.edu.cn; mdai@xmu.edu.cn

https://doi.org/10.1038/s41558-026-02559-3

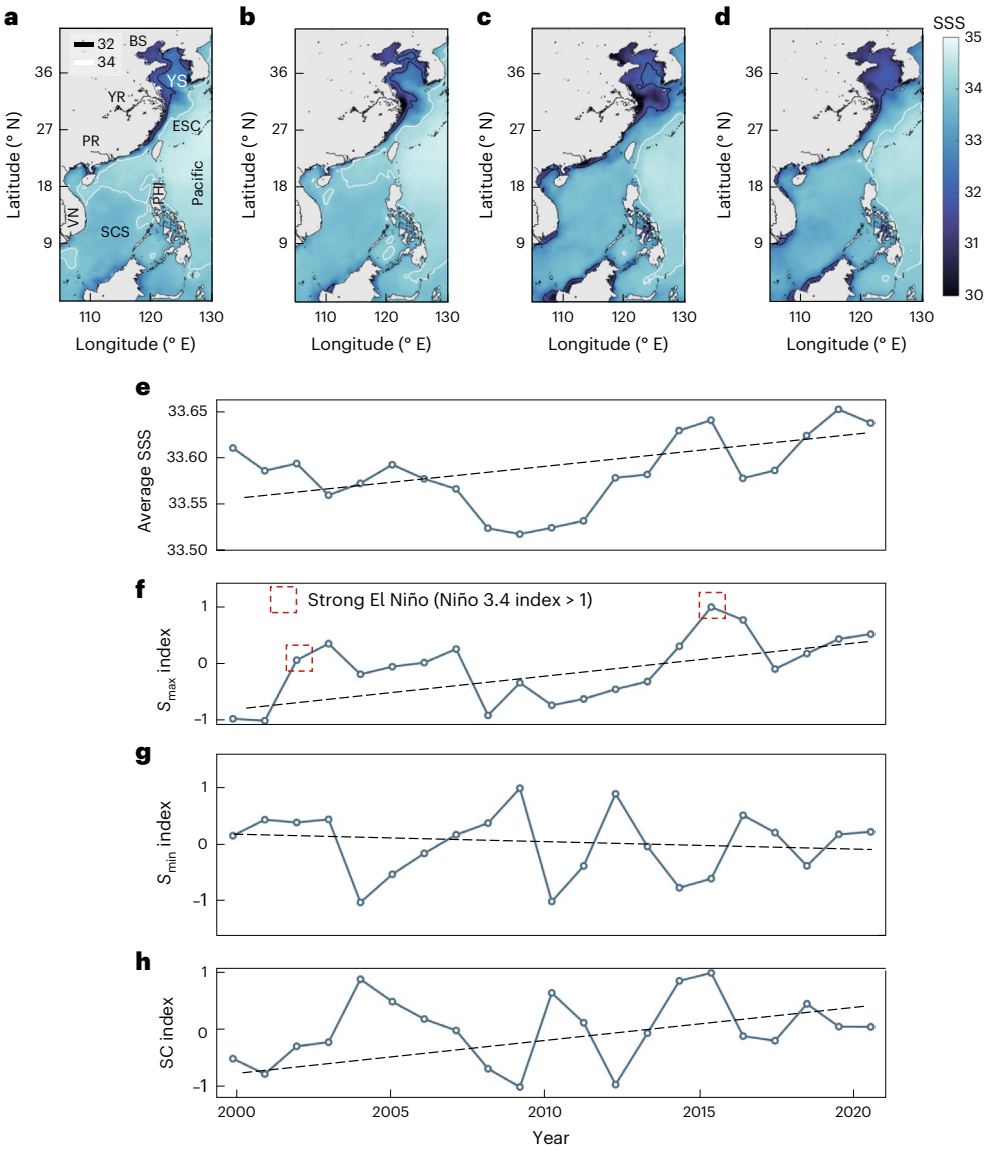


**Fig. 1 | Spatiotemporal variability of SSS in the China Seas. a–d**, Reconstructed long-term seasonal mean SSS fields from 2000 to 2020 for winter (**a**), spring (**b**), summer (**c**) and autumn (**d**). **e–h**, Interannual variations of key salinity metrics: average SSS (**e**), $S_{max}$ (**f**), $S_{min}$ (**g**) and SC (**h**) indices. BS, Bohai Sea; CJR, Changjiang River; ECS, East China Sea; PR, Pearl River; PHI, the Philippines; SCS, South China Sea; VN, Vietnam; YS, Yellow Sea. $S_{max}$ and $S_{min}$ can track the high (ocean-dominated) and low (river-dominated) salinity regimes, respectively, and thereby capture spatially varying influences of Kuroshio intrusion and river discharges.

Sea and the South China Sea, are characterized by highly productive fisheries, contributing nearly 20% of global fish capture[17]. The sea surface salinity (SSS) is highly variable (15–34.5) due to local and regional processes such as river plumes from the Changjiang and Pearl Rivers[18], monsoon-driven mixing and upwelling, Kuroshio intrusion and mesoscale eddies[15,16,18]. Such complexity presents notable challenges for both model simulations and satellite retrievals of SSS[19] (Supplementary Fig. 1) and hinders identification of key drivers of SSS variability as well as subsequent assessments of its impacts on fisheries.

Here using a newly reconstructed monthly SSS dataset for the China Seas and adjacent western Pacific (105–130° E, 0–42° N; Fig. 1a) in 2000–2020, we conceptualize the SSS field as a complex system marked by high spatiotemporal heterogeneity and nonlinear interactions. Using an eigen microstates approach[20], we identify the dominant modes and key processes regulating SSS variability in the China Seas. Under projected ENSO intensification, amplified inhomogeneous SSS variations may restructure regional fisheries in this ecologically critical region.

## Seasonal and interannual variations of SSS in the China Seas

The reconstructed SSS data (see Methods and Supplementary Information Sections 1–3 for details of reconstruction procedure and validation) effectively capture the complex spatiotemporal variability of SSS across the China Seas, including characteristic seasonal patterns driven by the East Asian monsoon and pronounced interannual changes (Fig. 1).

On the seasonal scale, the SSS peaks in winter (an average of 34.04), when the 34 isohaline extends westward to the Vietnam coast (Fig. 1a). Concurrently, the winter monsoon-driven China Coastal Current transports low-salinity Changjiang plume water southward into the northern South China Sea and delivers terrestrial nutrients critical for coastal fisheries[21]. In spring, the Kuroshio intrusion reduces[22], leading to a contraction of the 34 isohaline and the SSS declines basin-wide except along the southeastern coast of China, where the 32 isohaline retreats northward (Fig. 1b) due to weakened monsoons and China Coastal Current[18,23]. Meanwhile, the Changjiang River discharge increases[24],

pushing the 32 isohaline eastward. During summer, the SSS reaches its minimum (an average of 33.52) with the 32 isohaline widespread along the China coast and the 34 isohaline retreating entirely from the South China Sea and much of the East China Sea (Fig. 1c). The most pronounced freshening occurs off the Changjiang estuary and extends northward into the Bohai Sea and the Yellow Sea. Meanwhile, wind-driven coastal upwelling systems, such as the Vietnam upwelling (10–15° N, 110–114° E), Qiongdong upwelling (18.5–20.5° N, 111.5° E) and eastern Guangdong upwelling (23° N, 117° E), are most active, elevating SSS locally by the outcrop of more saline subsurface waters[25] and amplifying the spatial heterogeneity of the SSS with a standard deviation of 1.02 in the South China Sea. The fall season marks a transitional phase, with the 34 isohaline re-intruding the South China Sea (Fig. 1d).

On the interannual scale, the China Seas exhibit complex salinity dynamics characterized by a non-monotonic trend. Specifically, the SSS shows a significant decline from 2000 to 2010 ($-0.08 \pm 0.02$ decade$^{-1}$, $P < 0.01$), followed by an accelerating increase after 2010 ($0.11 \pm 0.03$ decade$^{-1}$, $P < 0.01$; Fig. 1e). These temporal changes of the mean SSS are coherent with the $S_{max}$ index ($r = 0.56$, $P < 0.01$; see Methods for $S_{max}$). The Kuroshio is a primary conduit between the China Seas and the western Pacific characterized by high salinity[21,26], so its intrusion is the dominant regulator of $S_{max}$. The significant correlation between $S_{max}$ and average SSS implicates Kuroshio intrusion as the principal driver of decadal-scale SSS variability. On average, regions contributing to $S_{max}$ cover approximately 66% of the China Seas, underscoring its relevance as a robust indicator of large-scale oceanic forcing. The parameter $S_{max}$ remains relatively stable with time (standard deviation, $\sigma = 0.018$). However, two notable surges appear in 2002–2003 and 2015, which coincide with El Niño (Fig. 1f), reflecting periods of intensified Kuroshio intrusion and elevated SSS in the China Seas[21].

By contrast, $S_{min}$ (see Methods for $S_{min}$) shows greater interannual variability ($\sigma = 0.041$). Notable troughs align with extreme hydrological events, including widespread flooding during 2003–2004 across eastern China[27], the catastrophic 2010 floods[28] and the 2015 ENSO-driven precipitation anomalies[29], each generating expansive freshwater plumes (Fig. 1g). A gradual rise in $S_{min}$ from 2004 to 2009 coincides with the completion of the Three Gorges Dam on the Changjiang River[30] and its decreasing river discharge[30,31]. The significant negative correlation between $S_{min}$ and the discharge during this period ($r = -0.83$, $P < 0.05$, Supplementary Fig. 12) indicates anthropogenic regulation of $S_{min}$, although quantitative differentiation of the effect is not likely with our data.

The salinity contrast index (SC index; see Methods for SC) quantifies the dynamic tension between high- and low-salinity domains[32] and provides a robust measure of hydrological changes[33]. It exhibits similarly great fluctuations ($\sigma = 0.042$) and is strongly correlated with $S_{min}$ ($r = -0.92$, $P < 0.01$), but not significant with $S_{max}$ ($r = 0.48$, $P > 0.5$), indicating that low-salinity dynamics predominantly shape nonlinear SSS gradients in the China Seas (Fig. 1h).

## ENSO drives salinity variability in the China Seas

To disentangle the key modes of SSS variability and their underlying drivers, we applied the eigen microstates approach to the dataset (Methods). The first three intrinsic modes, which explain ~32%, 12% and 7%, respectively, of the total variance, were retained for further analysis (Fig. 2). Their confidence intervals based on the North test do not overlap, indicating their statistical independence (Supplementary Fig. 13).

The first mode shows high temporal consistency (Fig. 2a) and its time series is significantly correlated with the evaporation minus precipitation ($E - P$) flux ($P < 0.05$, Fig. 2d), indicating that basin-scale SSS variability is primarily controlled by atmospheric freshwater fluxes. Negative anomalies along the southeastern coast of China, opposite the basin-scale $E - P$ mode, are caused by the winter monsoon-driven China Coastal Current, which carries low-salinity Changjiang River plume southward[21,34]. The second mode shows lower salinity near major estuaries (for example, the Changjiang and Pearl River estuaries) and higher values in the ocean basin, reflecting the influence of summer river plumes (Fig. 2b). Its time series is significantly positively correlated with the total river discharge (Fig. 2e), while negatively with the annual mean low SSS (SSS ≤ 30, Fig. 2k), confirming the dominance of river inputs. The third mode is characterized by a band of positive values extending from the eastern Philippines to the Okinawa Trough along the outer edge of the East China Sea, closely aligning with the pathway of the Kuroshio and its intrusions into the South China Sea and the East China Sea[26] (Fig. 2c). Its time series is significantly correlated with the sum of the Kuroshio intrusion velocities into the two seas (Fig. 2f), confirming that the highly saline water from the Kuroshio significantly affects the spatial variability of SSS in the China Seas. When the Kuroshio intrusion intensifies, the third mode increases and the SSS in the ocean basin gets higher (Fig. 2l). Thus, this mode represents the advection of high-salinity Kuroshio waters into the China Seas.

Together, the $E - P$ flux, river discharge and Kuroshio intrusion jointly regulate the variability of SSS across the China Seas. The basin-mean SSS increases with the sum of the three modes (Fig. 2i), while intra-annual SSS variability decreases (Fig. 2j). This inverse relationship reflects contrasting water mass behaviours: high-salinity oceanic waters tend to be more stable[26], whereas low-salinity coastal waters are temporally more variable because of dynamic local processes such as river plumes and upwelling[21]. In addition, all three modes and their dominant processes are significantly correlated with the Niño 3.4 index ($P < 0.05$, Fig. 2d–g), suggesting that ENSO modulates SSS variability in the China Seas through several pathways.

During El Niño (Niño 3.4 index of ≥0.5 °C), central-Pacific warming reorganizes the Walker Circulation, triggering subsidence and low-level divergence over the Philippine Sea that initiates the western North Pacific anomalous anticyclone[35,36]—a feature sustained into the following summer[37]. As observationally validated, the South China Sea-centred anticyclone suppresses convection, reduces precipitation and enhances evaporation, thereby elevating $E - P$ flux and salinity[35,37–39] (Figs. 3b,c and 4a). Convergent cross-mapping analysis (Methods) confirms robust causality from ENSO to $E - P$ flux to the first mode (skill score >0.30, $P < 0.05$, Extended Data Fig. 1a,b). Southerly winds from the anticyclone transport moisture to the mainland of China, where convergence and uplift occur upon colliding with Siberian cold air across southern and eastern China[37] (Fig. 3a). This air uplift leads to enhanced precipitation in southern China. The persisting anticyclone, sustained by developing ENSO conditions[37], maintains southerly flow along southeastern China, driving continuous precipitation[40] (Fig. 3b) and thereby enhancing river discharge, especially for the Changjiang and Pearl Rivers, subsequently decreasing the SSS in river-dominated regions[41] (Figs. 3c and 4c). These precipitation-driven changes regulate the spatial distribution of SSS, consistent with the spatiotemporal shifts observed in the second mode. Convergent cross-mapping analysis confirms causal convergence from ENSO to river discharge to the second mode (skill score >0.40, $P < 0.05$, Extended Data Fig. 1d,e). Additionally, the anticyclone weakens wind-driven coastal upwelling, such as the Qiongdong, Vietnam and Luzon upwelling[42,43], which limits the upward transport of more saline subsurface water, leading to anomalously low SSS in these regions[44] (Fig. 3c). North Equatorial Current bifurcation migrates northward, weakening the Kuroshio, but enhancing its westward intrusion into the South China Sea[42,45], which offsets the freshening from weakened upwelling in the intrusion pathway (Figs. 3c and 4e). Strengthened mid-latitude westerlies enhance the Kuroshio intrusion in the East China Sea via a negative wind stress curl[46], thereby introducing more highly saline waters to the region. Therefore, El Niño can lead to an increase in the SSS in ocean-dominated margins. Convergent cross-mapping analysis confirms the causal convergence from ENSO to Kuroshio intrusion in the South China Sea/East China Sea

https://doi.org/10.1038/s41558-026-02559-3

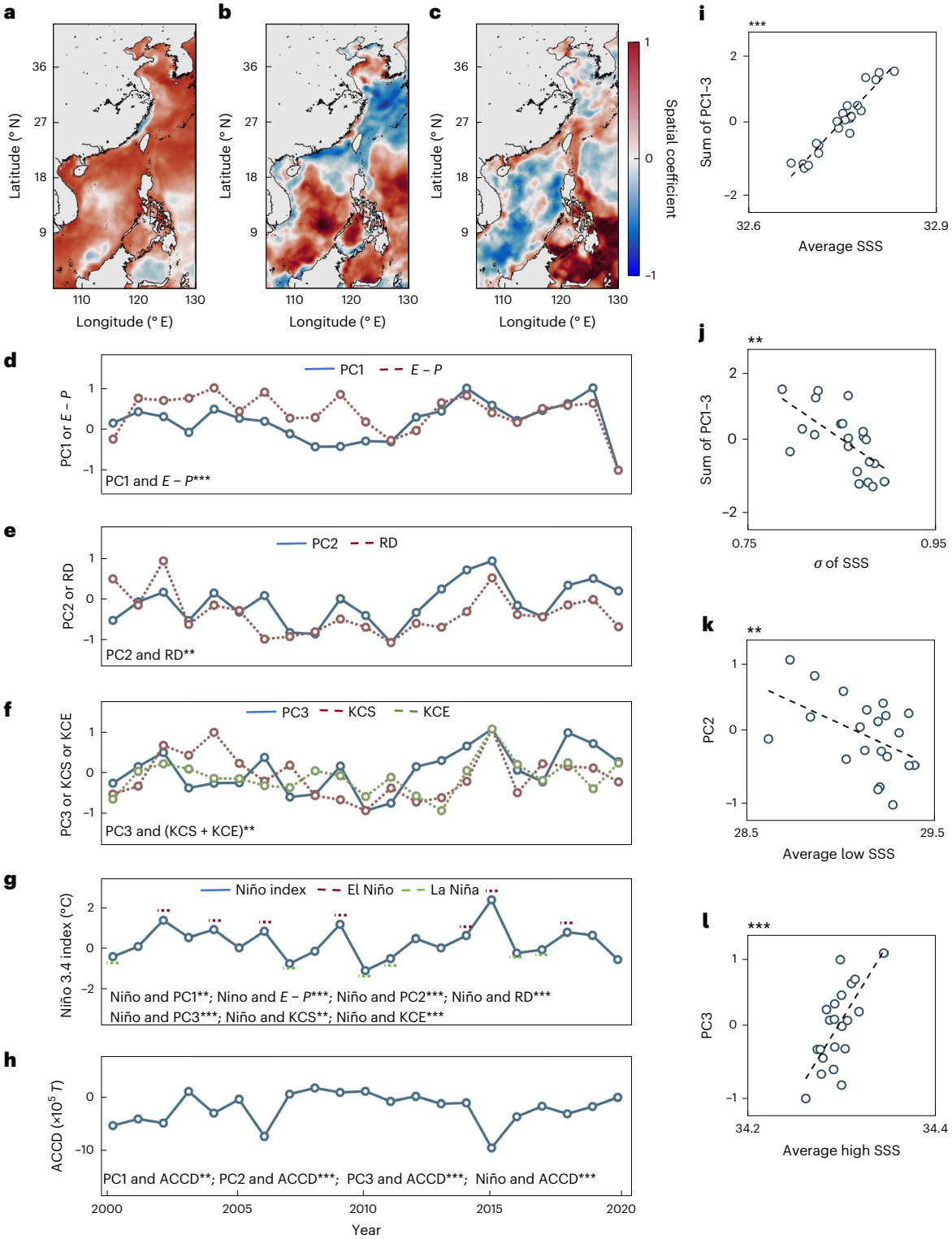


**Fig. 2 | The eigen microstates approach reveals dominant drivers of SSS variability in the China Seas. a**–**c**, Spatial patterns of leading modes: first mode (**a**), second mode (**b**) and third mode (**c**). **d**–**f**, Normalized principal component time series (PCs, averaged from June of each year to May of the following year) and the corresponding dominant physical drivers: PC1 and evaporation minus precipitation flux ($E-P$) (**d**), PC2 and river discharge (RD) (**e**), and PC3 and Kuroshio intrusion velocities into the South China Sea (KCS) and East China Sea (KCE) (**f**). **g**, Annual Niño 3.4 index (averaged over June–December). **h**, The annual change in the north–south catch differences in total marine fisheries recorded in China Fisheries Yearbooks (ACCD). **i**–**l**, Relationships between annual mean SSS (**i**), intra-annual SSS variability (**j**), annual mean low (SSS ≤ 30) SSS and normalized PCs (**k**) and high (SSS ≥ 34) SSS and normalized PCs (**l**). Positive ACCD indicates increasing catch difference favouring the north. Since ACCD shows a 1-year lag response to the Niño 3.4 index (Supplementary Fig. 14), ACCD here is 1-year lag corrected. For example, the ACCD value for 2015 represents the north–south catch difference between 2016 and 2015. In **d**–**l**, ***$P < 0.01$; **$0.01 < P < 0.05$. The Pearson correlation coefficients and $P$ values are provided in Extended Data Table 1. RD and Kuroshio velocity apparently correlate less strongly with the basin-scale modes than the basin-wide $E-P$ flux, as they are local/regional processes. These significant correlations suggest an ENSO forcing–salinity–fishery positive feedback.

https://doi.org/10.1038/s41558-026-02559-3

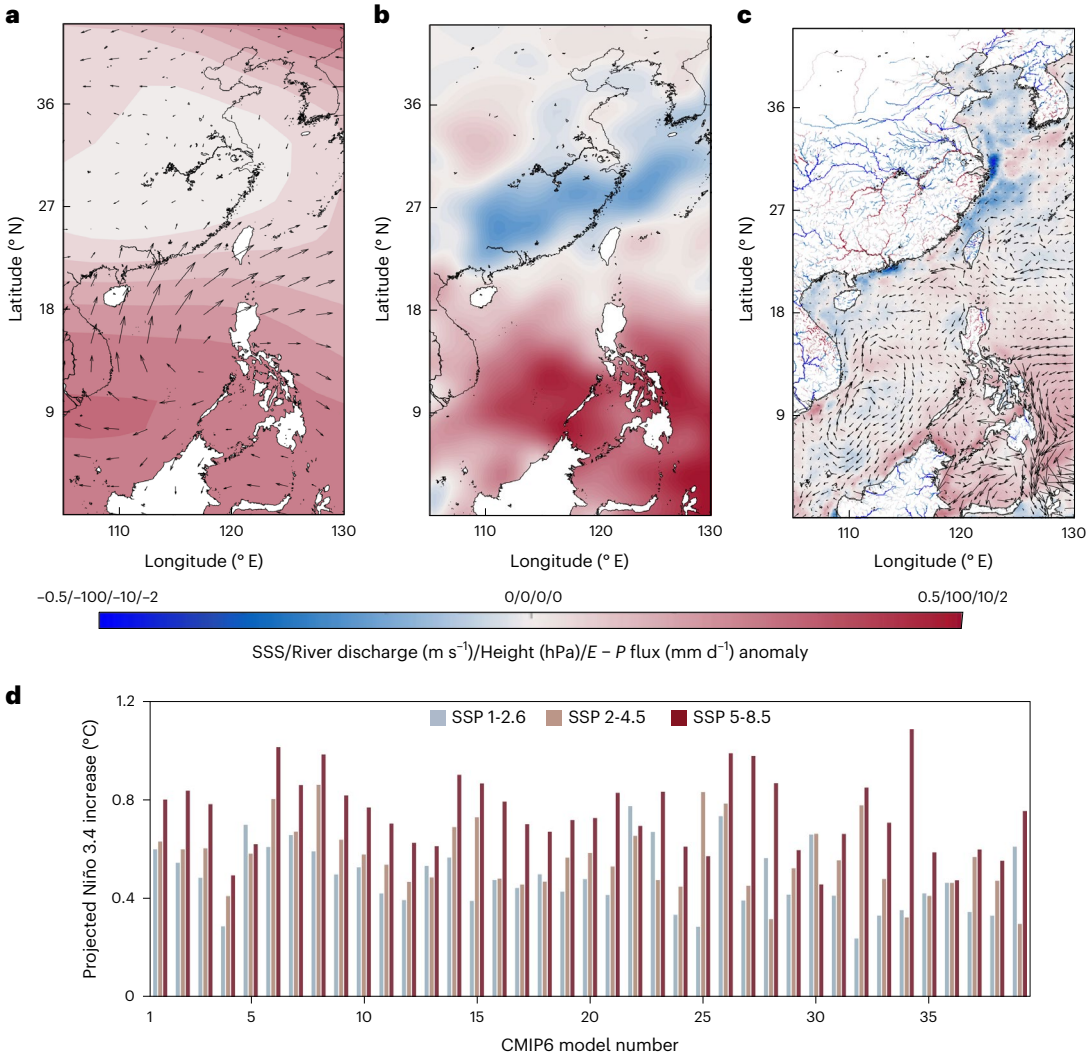


**Fig. 3 | Spatial anomalies associated with El Niño events during 2000–2020 and projected increases in the Niño 3.4 index under future emission scenarios by various CMIP6 models. a**, Geopotential height anomaly (filled contours) and wind anomaly (arrows) relative to the 2000–2020 climatological baselines. **b**, Evaporation minus precipitation ($E-P$) flux anomaly. **c**, SSS anomalies (filled contours over ocean) and river discharge anomalies (filled contours on land), align with surface circulations anomalies (arrows) in the China Seas and western Pacific. **d**, Projected increases in the Niño 3.4 index from 2020 to 2100 under shared socioeconomic pathways SSP 1-2.6, SSP 2-4.5 and SSP 5-8.5, relative to the 2000–2020 climatological mean, simulated by 39 CMIP6 models. The bootstrap test at the 95% confidence level indicates that most regions in **a**–**c** show statistically significant results (Supplementary Fig. 15). Details of 39 CMIP6 models are provided in Supplementary Table 8. All models project an increase in the Niño 3.4 index over the coming decades.

to the third mode (skill score >0.30, $P < 0.05$, Extended Data Fig. 1g,h). Thus, El Niño drives coastal SSS freshening via river discharge and basin-wide SSS increasing through enhanced $E-P$ flux/Kuroshio intrusion, amplifying spatial salinity contrast, which is consistent with the Clausius–Clapeyron expectation under global warming[4].

On the contrary, during La Niña (Niño 3.4 index ≤−0.5 °C), the anomalous western North Pacific cyclone over the South China Sea enhances precipitation, lowering basin-scale SSS[47,48] (Fig. 4b). Meanwhile, the cyclone-driven northerly winds over China reduce precipitation and river discharge, elevating estuarine and coastal salinity[47,48] (Fig. 4d). The Kuroshio intrusion weakens as a result of the southward shift of the North Equatorial Current bifurcation[49,50], bringing about less advection of highly saline water (Fig. 4f).

Projections from 39 Coupled Model Intercomparison Project Phase 6 (CMIP6) models under high emission scenarios suggest that the Niño 3.4 index will rise by 0.4 °C to 0.8 °C by 2100 (Fig. 3d). Intensified ENSO is likely to enhance the modulation of $E-P$ flux, river discharge and Kuroshio intrusion, thereby amplifying salinity inhomogeneity across the China Seas in the coming decades.

## Impacts of ENSO-driven salinity variations on fishery

The SSS anomalies in 2000–2020 show a zonal dipole during El Niño. It decreases in most low-SSS regions (SSS ≤ 30) and about 50% of the high-SSS regions (SSS ≥ 34), while increases in the remaining areas (Fig. 5). Specifically, it increases with greater temporal fluctuations in the South China Sea, while decreases in most areas of the northern China Seas with less temporal fluctuations in most of the Bohai Sea and the Yellow Sea north of 35° N (Fig. 5a,b).

The significant negative correlation ($P < 0.05$, Extended Data Fig. 2) between the Niño 3.4 index and the annual change in the north–south catch differences in total marine fishery (ACCD, where the south includes the South China Sea and the north includes the East China Sea, the Yellow Sea and the Bohai Sea) suggests that ENSO regulate fishery resources in China's coastal waters. For example, ACCD declined during El Niño in 2002, 2004, 2006 and 2015, but rose during La Niña in 2005, 2007, 2010 and 2017 (Fig. 2g,h). Notably, this correlation is sea surface temperature-independent ($P > 0.5$), but links strongly to the first three SSS modes (precipitation, river discharge and Kuroshio intrusion;

https://doi.org/10.1038/s41558-026-02559-3

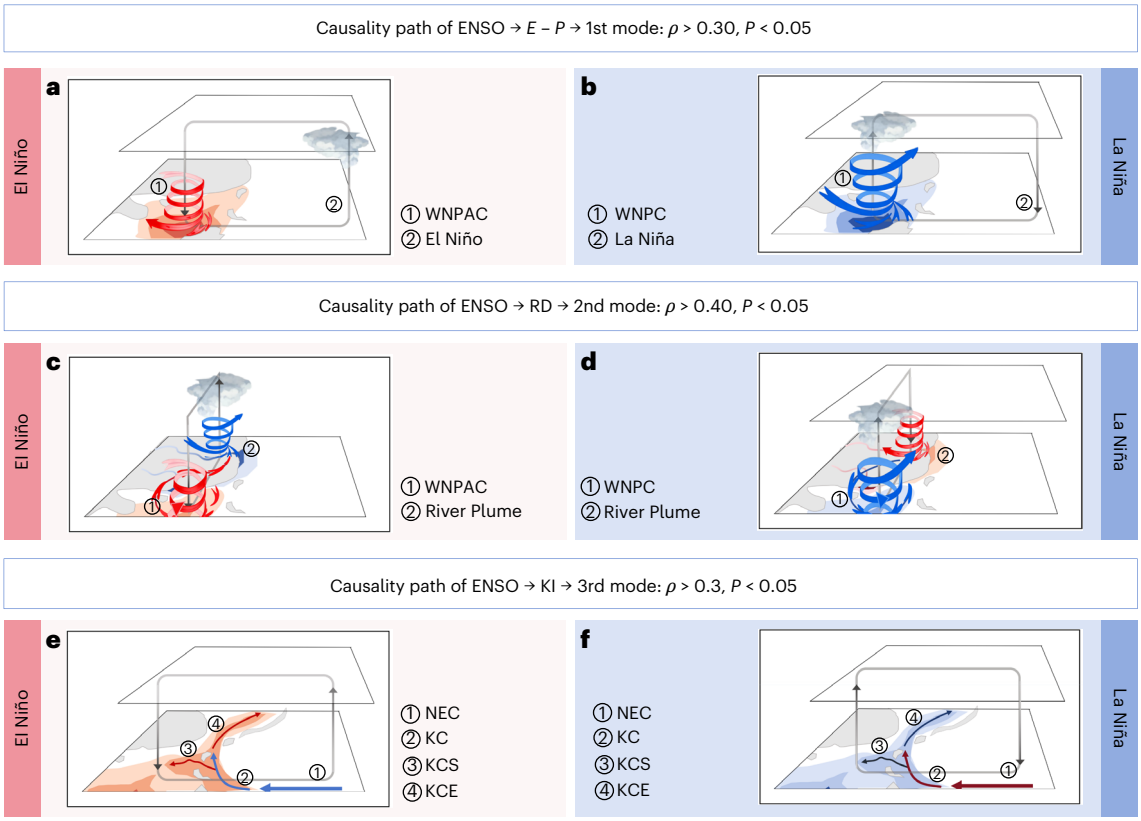


**Fig. 4 | Causality pathways of ENSO impacts on SSS. a**,**b**, ENSO influences evaporation–precipitation flux ($E - P$), driving the first mode of salinity through the western North Pacific anomalous anticyclone (WNPAC) (**a**)/cyclone (WNPC) (**b**) (WNPAC/WNPC). **c**,**d**, ENSO alters RD, regulating the second mode of salinity via increased (**c**)/decreased (**d**) precipitation anomalies and freshwater inputs from major rivers. **e**,**f**, ENSO modulates the Kuroshio intrusion (KI), shaping the third mode of salinity by enhancing (**e**) or weakening (**f**) saline inflows into the South and East China Seas. KC, Kuroshio Current; KCS and KCE, Kuroshio intrusions in the South China Sea and the East China Sea, respectively; NEC, North Equatorial Current. Parameter $\rho$ is the skill score of convergent cross-mapping analysis. All pathways are confirmed by significant convergence ($\rho > 0.30$, $P < 0.05$; Extended Data Fig. 1).

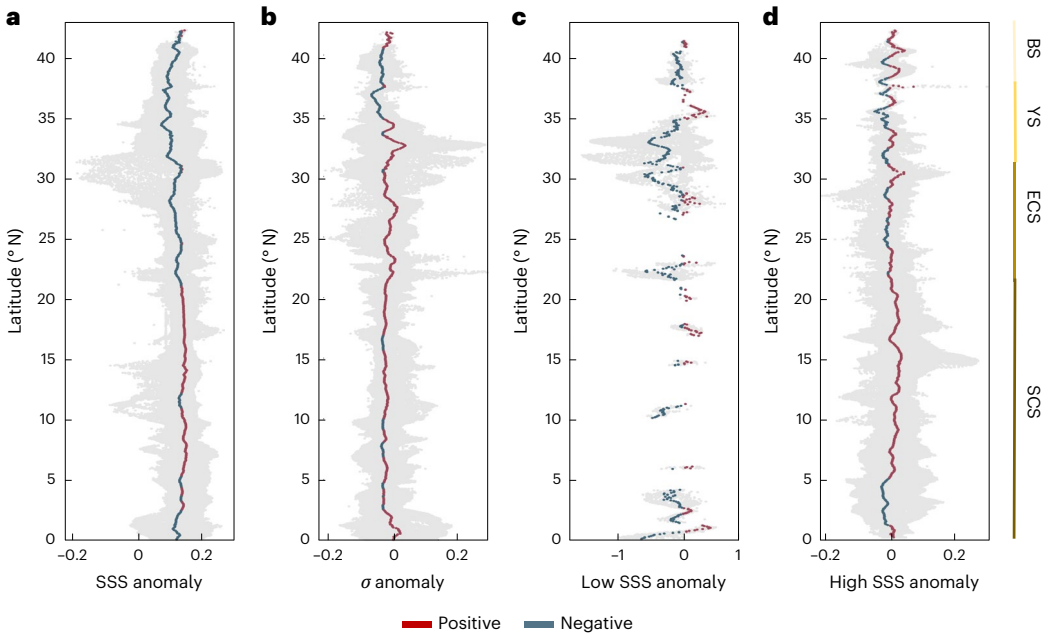


**Fig. 5 | Zonal-mean SSS anomalies highlight distinctive dipoles during El Niño events relative to the climatological baselines. a**,**b**, Zonal-mean SSS anomalies (**a**) and their variability (**b**). **c**,**d**, SSS anomalies in river-dominated low SSS (SSS ≤ 30) region (**c**) and ocean-dominated high SSS (SSS ≥ 34) region (**d**). The shaded areas represent uncertainty ranges derived from all the data. Zonal-mean anomalies are averages of the temporal means from June of an El Niño year to May of the following year across 105–130° E for each 0.05° latitude band (not a single transect).

https://doi.org/10.1038/s41558-026-02559-3

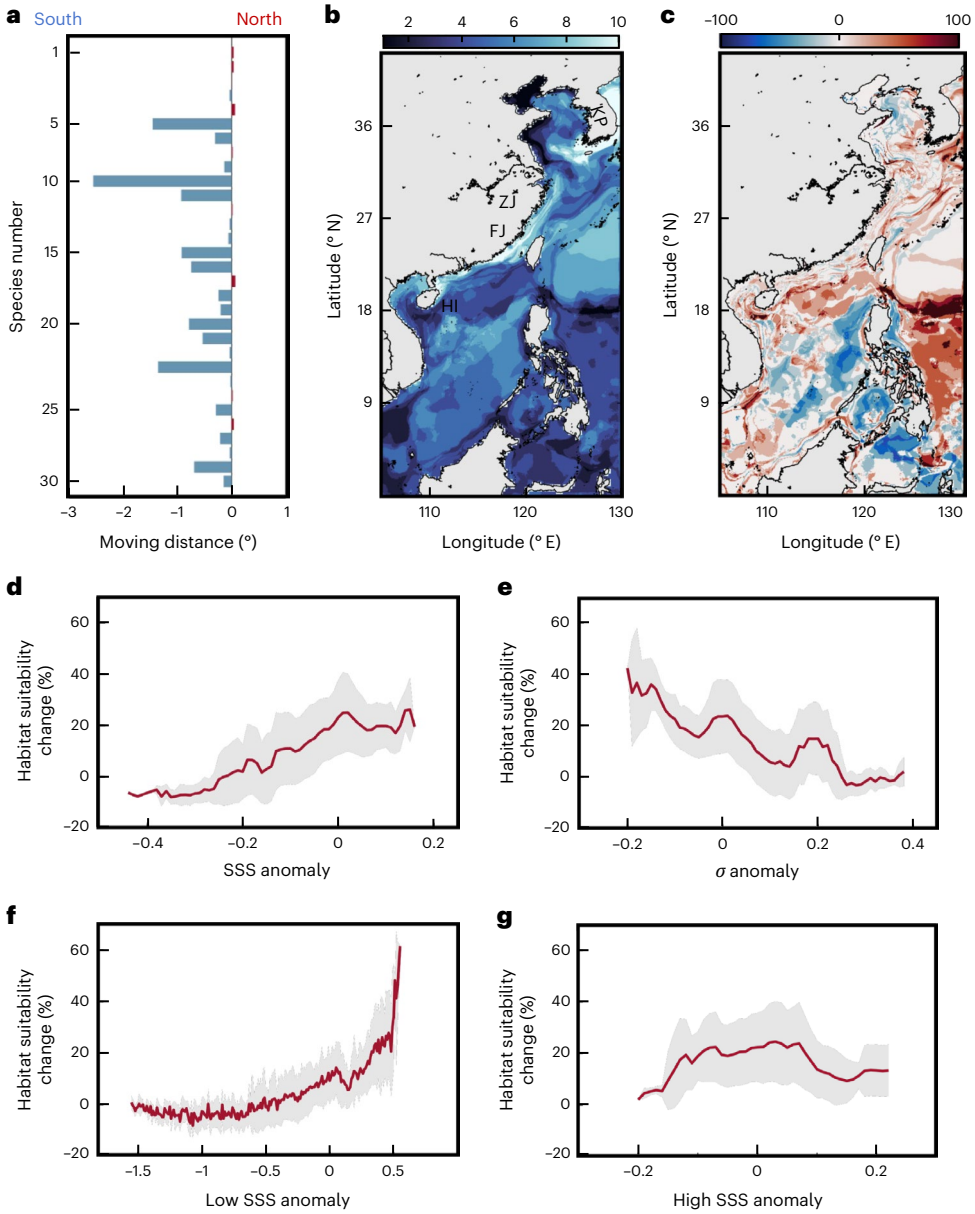


**Fig. 6 | Southward migration of fish species and changes in species richness in response to SSS variations during El Niño years in the China Seas. a**, Centroid shifts of individual species during El Niño years, with negative indicating southward and positive northward. **b**, Climatological distribution of species richness. **c**, Changes in species richness (percentage) during El Niño years relative to climatological baselines. **d**–**g**, Changes in habitat suitability associated with SSS anomalies; linear correlation coefficients 0.95 ($P = 0.001$) (**d**), −0.91 ($P = 0.001$) (**e**), 0.80 ($P = 0.001$) (**f**) and 0.09 ($P = 0.653$) (**g**). The correlation analyses in **f** and **g** were performed using the suitability changes ($n = 400$) corresponding to the low- and high-SSS grid cells, respectively, based on a two-sided $t$-test. The shaded areas represent 1$\sigma$ uncertainty ranges. Results are based on the species-distribution model. FJ, Fujian Province; HI, Hainan Island; KP, Korean Peninsula; ZJ, Zhejiang Province.

$P < 0.05$, Fig. 2), connecting ENSO and salinity to ACCD. Convergent cross-mapping analysis confirms the causal links from ENSO to salinity and then to fishery (Extended Data Figs. 1 and 3).

We thus propose an ENSO forcing–salinity–fishery positive feedback hypothesis: the coupling of ocean–atmosphere dynamics during El Niño, mediated by the Western North Pacific anomalous anticyclone, generates spatially inhomogeneous salinity anomalies through concurrent changes in $E - P$ flux, river discharge and Kuroshio intrusion, which induce fish migration and ultimately influence fishery production. Results from a species-distribution model (Methods) support this hypothesis. Salinity-induced ecological shifts drive southward relocation of commercial fish habitats (Fig. 6a), consistent with observed ACCD declines ~1 year after El Niño (Fig. 2g,h). Climatologically, species richness peaks along the China coast from south of the Changjiang estuary to Hainan Island and around the southern Korean Peninsula (Fig. 6b). Model results encode species-specific salinity tolerance and regional responses, showing habitat anomalies during El Niño that mirror observed salinity patterns (Extended Data Fig. 4). El Niño drives overall southward shift of fish habitats and enhances habitat suitability across much of the China Seas except some areas of the central South China Sea (Fig. 6c and Extended Data Fig. 4), where local richness declines because intensified salinity anomalies cause habitat suitability to drop below the survival threshold (Extended Data Fig. 4). These declines are most pronounced in major coastal upwelling systems, such as the Vietnam and Luzon upwelling. The weakening of upwelling during El Niño reduces vertical nutrient supply and lowers

subsurface salinity contributions, exacerbating the decline in fish biodiversity[39,44] (Fig. 3c). Species richness decreases in the Bohai Sea and northern Yellow Sea, consistent with the southward shift of commercial fish species (Fig. 6a–c and Extended Data Fig. 4). By contrast, coastal waters off Zhejiang and Fujian provinces experience increases in species richness (Fig. 6c and Extended Data Fig. 4).

Overall, El Niño-induced salinity variations clearly link to shifts in marine habitat suitability (Fig. 6d–g). At the ecosystem level, habitat suitability correlates positively with the average SSS anomaly (Fig. 6d), but negatively with anomaly variability ($\sigma$ of SSS anomaly, Fig. 6e), as the 31 commercial fish species thrive in stable high-salinity environments (Supplementary Table 9). In river-dominated low-SSS zones, habitat suitability gradually increases with SSS anomaly when the anomaly is negative (Fig. 6f), similar to the overall average SSS anomaly (Fig. 6d). When SSS is close to 30, however, the habitat suitability surges (Fig. 6f). By contrast, in ocean-dominated high-salinity regions, habitat suitability shows almost symmetric responses to salinity anomalies: positive for negative anomalies, while negative for positive anomalies (Fig. 6g). This symmetry arises from the salinity–nutrient paradox in high-salinity regions: although marine fish species exhibit physiological preference for saline waters, further increase in salinity reflects stronger intrusion of oligotrophic open-ocean waters, a process that simultaneously dilutes bioavailable nutrients. In principle, the habitat redistribution may arise from three synergistic effects: (1) species-specific salinity tolerance thresholds, (2) trophic enhancement via riverine nutrients in low-SSS coastal waters and (3) habitat degradation in high-salinity regions caused by reduced carrying capacity. These effects are observationally and experimentally validated among 31 species (Supplementary Table 9). Consequently, fish species have to optimize their ecological niches by balancing osmoregulatory advantages against trophic constraints, ultimately establishing population viability thresholds where critical salinity and nutrient concentrations intersect.

## Remarks and implications

Our findings establish the dual roles of ENSO as both a remote driver and regional amplifier of SSS inhomogeneity in the China Seas, highlighting the complexity of the response of SSS to climate change. This mechanistic understanding complements existing views that emphasize the role of surface freshwater fluxes ($E - P$) in shaping inhomogeneous SSS in marginal seas. Our analysis further reveals that ENSO-induced SSS variations drive a latitudinal shift in fishery production within the China Seas. For instance, Shandong Province (in the northern China Seas) reported a 6% decline in fishery capture revenue in strong El Niño years over the past two decades, while Guangdong Province (in the southern China Seas) saw a 15% increase[51]. CMIP6 climate models project a 40-70% increase in the intensity of extreme ENSO by 2100[52] (Fig. 3b). This could intensify both mean SSS levels and salinity contrast across the region according to their significant positive correlations (Fig. 2), resulting in a projected 15–25% decline in ACCD. These implications mainly reflect El Niño conditions, with more limited inference regarding La Niña. Thus, ENSO-driven inhomogeneous salinity patterns and subsequent fish migration may shift the geographic focus of China's fishing industry over the coming decades, potentially reshaping its spatial and economic landscapes.

Notably, although ENSO-driven inhomogeneous SSS variations may shift China's fishery focus southward, this spatial displacement cannot be equated with reduction of fishery production. Chinese marine fishery catch increased from 2011 to 2016, peaking during strong El Niño of 2015–2016[51]. This increase can be mainly attributed to intensified fishing effort and salinity (~70% variance explained) based on generalized additive models[13], as well as to enhanced fish habitat suitability under inhomogeneous salinity variations primarily driven by ENSO as inferred from the causal tests (Extended Data Figs. 1 and 3). In contrast, such inhomogeneous SSS variations may reduce habitat suitability of fish in the South China Sea (Fig. 5c), consistent with sharp catch declines of 10–15% in Indonesia and the Philippines during 2015–2016 El Niño[17]. Given that fisheries play critical roles in the gross domestic products of Indonesia and the Philippines and support over 25 million livelihoods, ENSO-modulated SSS inhomogeneity could fundamentally alter marine resource distributions. This may exacerbate socioeconomic disparities in fishery-dependent regions, challenging progress towards sustainable development goal 14 (life below water).

## Online content

Any methods, additional references, Nature Portfolio reporting summaries, source data, extended data, supplementary information, acknowledgements, peer review information; details of author contributions and competing interests; and statements of data and code availability are available at https://doi.org/10.1038/s41558-026-02559-3.

## References


1. Curry, R., Dickson, B. & Yashayaev, I. A change in the freshwater balance of the Atlantic Ocean over the past four decades. *Nature* **426**, 826–829 (2003).
2. Durack, P. J., Wijffels, S. E. & Matear, R. J. Ocean salinities reveal strong global water cycle intensification during 1950 to 2000. *Science* **336**, 455–458 (2012).
3. Lu, Y. et al. North Atlantic–Pacific salinity contrast enhanced by wind and ocean warming. *Nat. Clim. Change* **14**, 723–731 (2024).
4. Bindoff, N. L. et al. in *Climate Change 2007: The Physical Science Basis* (eds Solomon, S. et al.) 385–432 (Cambridge Univ. Press, 2007).
5. Cravatte, S., Delcroix, T., Zhang, D., McPhaden, M. & Leloup, J. Observed freshening and warming of the western Pacific Warm Pool. *Clim. Dynam.* **33**, 565–589 (2009).
6. Durack, P. J. & Wijffels, S. E. Fifty-year trends in global ocean salinities and their relationship to broad-scale warming. *J. Clim.* **23**, 4342–4362 (2010).
7. Sallée, J.-B. et al. Summertime increases in upper-ocean stratification and mixed-layer depth. *Nature* **591**, 592–598 (2021).
8. Arnér, M. & Koivisto, S. Effects of salinity on metabolism and life history characteristics of *Daphnia magna*. *Hydrobiologia* **259**, 69–77 (1993).
9. Smyth, K. & Elliott, M. in *Stressors in the Marine Environment* (eds Solan, M. & Whiteley, N.) 161–174 (Oxford Univ. Press, 2016).
10. Kültz, D. The combinatorial nature of osmosensing in fishes. *Physiology* **27**, 259–275 (2012).
11. Song, J. A., Choi, Y. J. & Choi, C. Y. Effects of salinity changes on the osmoregulatory and stress responses in the bay scallop *Argopecten irradians*. *Fish. Sci.* **88**, 275–283 (2022).
12. Hong, X. et al. Effects of climate events on abundance and distribution of major commercial fishes in the Beibu Gulf South China Sea. *Diversity* **15**, 649 (2023).
13. Li, M. et al. Impacts of strong ENSO events on fish communities in an overexploited ecosystem in the South China Sea. *Biology* **12**, 946 (2023).
14. Zhang, Y. et al. Indian Ocean Dipole and ENSO's mechanistic importance in modulating the ensuing-summer precipitation over Eastern China. *npj Clim. Atmos. Sci.* **5**, 48 (2022).
15. Liu, J., Bellerby, R. G. J., Zhu, Q. & Ge, J. Estimating sea surface salinity in the East China Sea using satellite remote sensing and machine learning. *Earth Space Sci.* **10**, e2023EA003230 (2023).
16. Zeng, L. et al. Decadal variation and trends in subsurface salinity from 1960 to 2012 in the northern South China Sea. *Geophys. Res. Lett.* **43**, 12 (2016).
17. FAO. *Fishery and Aquaculture Statistics. Global Production by Production Source 1950–2021 (FishStatJ)* (FAO Fisheries and Aquaculture Division: Rome, 2023).

18. Zhang, C., Huang, Y. & Ding, W. Enhancement of Zhe-Min coastal water in the Taiwan Strait in winter. *J. Oceanogr.* **76**, 197–209 (2020).
19. Yu, L. A global relationship between the ocean water cycle and near-surface salinity. *J. Geophys. Res.* **116**, C10025 (2011).
20. Hu, G., Liu, T., Liu, M., Chen, W. & Chen, X. Condensation of eigen microstate in statistical ensemble and phase transition. *Sci. China Phys. Mech. Astron.* **62**, 990511 (2019).
21. Wang, Z., Wang, G., Guo, X., Hu, J. & Dai, M. Reconstruction of high-resolution sea surface salinity over 2003–2020 in the South China Sea using the machine learning algorithm LightGBM model. *Remote Sens.* **14**, 6147 (2022).
22. Centurioni, L. R., Niiler, P. P. & Lee, D.-K. Observations of inflow of Philippine sea surface water into the South China Sea through the Luzon Strait. *J. Phys. Oceanogr.* **34**, 113–121 (2004).
23. Loo, Y. Y., Billa, L. & Singh, A. Effect of climate change on seasonal monsoon in Asia and its impact on the variability of monsoon precipitation in Southeast Asia. *Geosci. Front.* **6**, 817–823 (2015).
24. Cheng, P. Dispersal of the Changjiang River water in East Asian shelf seas. *J. Geophys. Res. Oceans* **129**, e2024JC021351 (2024).
25. Wang, D. et al. Relative contributions of local wind and topography to the coastal upwelling intensity in the northern South China Sea. *J. Geophys. Res. Oceans* **119**, 2550–2567 (2014).
26. Du, C. et al. Impact of the Kuroshio intrusion on the nutrient inventory in the upper northern South China Sea: insights from an isopycnal mixing model. *Biogeosciences* **10**, 6419–6432 (2013).
27. Lin, C. A. et al. Atmospheric–hydrological modeling of severe precipitation and floods in the Huaihe River Basin, China. *J. Hydrol.* **330**, 249–259 (2006).
28. Kundzewicz, Z. W. et al. Climate variability and floods in China—a review. *Earth Sci. Rev.* **211**, 103434 (2020).
29. Zhai, P. et al. The strong El Niño of 2015/16 and its dominant impacts on global and China's climate. *J. Meteorol. Res.* **30**, 283–297 (2016).
30. Lyu, J. et al. Extreme drought–heatwave events threaten the biodiversity and stability of aquatic plankton communities in the Yangtze River ecosystems. *Commun. Earth Environ.* **6**, 171 (2025).
31. Dai, Z., Du, J., Li, J., Li, W. & Chen, J. Runoff characteristics of the Changjiang River during 2006: effect of extreme drought and the impounding of the Three Gorges Dam. *Geophys. Res. Lett.* **35**, 2008GL033456 (2008).
32. Cheng, L. et al. Improved estimates of changes in upper ocean salinity and the hydrological cycle. *J. Clim.* **33**, 10357–10381 (2020).
33. IPCC. *Climate Change 2021—The Physical Science Basis* (eds Masson-Delmotte, V. et al.) (Cambridge Univ. Press, 2023).
34. Chen, C.-T. A. et al. Southward spreading of the Changjiang diluted water in the La Niña spring of 2008. *Sci. Rep.* **11**, 307 (2021).
35. Wang, B., Wu, R. & Fu, X. Pacific–East Asian teleconnection: how does ENSO affect East Asian climate?. *J. Clim.* **13**, 1517–1536 (2000).
36. Thual, S. & Dewitte, B. ENSO complexity controlled by zonal shifts in the Walker circulation. *Nat. Geosci.* **16**, 328–332 (2023).
37. Xie, S.-P. et al. Indian Ocean capacitor effect on Indo–Western Pacific climate during the summer following El Niño. *J. Clim.* **22**, 730–747 (2009).
38. Cai, W. et al. Pantropical climate interactions. *Science* **363**, eaav4236 (2019).
39. Qi, J. et al. Impacts of El Niño on the South China Sea surface salinity as seen from satellites. *Environ. Res. Lett.* **17**, 054040 (2022).
40. Wang, Z., Sun, J., Wu, J., Ning, F. & Chen, W. Attribution of persistent precipitation in the Yangtze-Huaihe River Basin during February 2019. *Adv. Atmos. Sci.* **37**, 1389–1404 (2020).
41. Park, T., Jang, C. J., Kwon, M., Na, H. & Kim, K.-Y. An effect of ENSO on summer surface salinity in the Yellow and East China Seas. *J. Mar. Syst.* **141**, 122–127 (2015).
42. Hu, D. et al. Pacific western boundary currents and their roles in climate. *Nature* **522**, 299–308 (2015).
43. Xie, L., Zong, X., Yi, X. & Li, M. The interannual variation and long-term trend of Qiongdong upwelling. *Chin. J. Oceanol. Limnol.* **47**, 43–51 (2016).
44. Xiu, P. et al. On contributions by wind-induced mixing and eddy pumping to interannual chlorophyll variability during different ENSO phases in the northern South China Sea. *Limnol. Oceanogr.* **64**, 503–514 (2019).
45. Wang, C., Wang, W., Wang, D. & Wang, Q. Interannual variability of the South China Sea associated with El Niño. *J. Geophys. Res.* **111**, 2005JC003333 (2006).
46. Wang, Y.-L., Jin, F.-F., Wu, C.-R. & Qiu, B. Northwestern Pacific Oceanic circulation shaped by ENSO. *Sci. Rep.* **14**, 11684 (2024).
47. Huang, G. et al. Seasonally evolving impacts of multiyear La Niña on precipitation in Southern China. *Front. Earth Sci.* **10**, 884604 (2022).
48. Zhang, R., Min, Q. & Su, J. Impact of El Niño on atmospheric circulations over East Asia and rainfall in China: role of the anomalous western North Pacific anticyclone. *Sci. China Earth Sci.* **60**, 1124–1132 (2017).
49. Qu, T. et al. Can Luzon Strait transport play a role in conveying the impact of ENSO to the South China Sea?. *J. Clim.* **17**, 3644–3657 (2004).
50. Wu, C., Hsin, Y., Chiang, T., Lin, Y. & Tsui, I. Seasonal and interannual changes of the Kuroshio intrusion onto the East China Sea Shelf. *J. Geophys. Res. Oceans* **119**, 5039–5051 (2014).
51. *China Fisheries Yearbooks 2001–2020* (Bureau of Fisheries, 2001–2020).
52. Cai, W. et al. Increased ENSO sea surface temperature variability under four IPCC emission scenarios. *Nat. Clim. Change* **12**, 228–231 (2022).

# Methods

## Machine learning for SSS reconstruction

We developed a machine learning algorithm that integrates remote-sensing data with an extensive cruise and buoy-based observational dataset to reconstruct SSS in the China Seas at a spatial resolution of 0.05° × 0.05° over the period of 2000–2020 with high accuracy. The reconstruction of SSS was conducted following two steps: (1) data processing and (2) model training and testing. In the first step, in situ observational data were gridded into 0.05° × 0.05° boxes at a monthly temporal resolution. Empirical orthogonal function analysis was used to impose spatial constraints on the reconstruction. The in situ SSS data and corresponding remote-sensing-derived data were then portioned into training (85%) and testing (15%) sets for model development. To ensure adequate representation of the coastal area in the training data, the South China Sea and the northern China Seas were divided into two regions along the 200-m and 50-m isobaths, respectively. Data from each region were split into training and testing sets with the same ratios (85%:15%) before being combined to form the final training and testing sets. It should be noted that all data used in model training were interpolated onto the same spatial grids.

For model development, we chose a robust machine learning algorithm for SSS retrieval. Subsequently, we used hyperparameter methods (codes from https://github.com/optuna/) to determine the optimal range of parameters for the training set. Final hyperparameter values were determined using *k*-fold cross validation (https://github.com/suryanktiwari/Linear-Regression-and-K-fold-cross-validation). The resulting optimized model was applied to the training data and its predictive performance was evaluated with the independent testing set. Various indicators of the accuracy of the model were calculated. The reconstructed SSS exhibits high accuracy, with a mean absolute error of 0.13 and a mean root mean square error of 0.22. All accuracy-evaluation metrics are based solely on the independent testing dataset.

Further details of the methods are provided in Supplementary Information Sections 2 and 3. The figures were created using MATLAB and Python.

## Definitions of $S_{max}$, $S_{min}$ and SC indices

The $S_{max}$ and $S_{min}$ indices represent the normalized, area-weighted mean of the salinity above and below the climatological mean ($S_{clim}$) and were calculated over dynamically defined domains relative to $S_{clim}$. The SC index, defined as the normalized difference between $S_{max}$ and $S_{min}$, quantifies the contrast between the relatively high- and low-salinity regimes.

## Eigen microstates approach

The approach extends Gibbs' ensemble theory from statistical physics to analyse the dynamics of complex systems[53–55]. In this framework, the state of a complex system at a given time is defined as its microstate, while the collection of all such microstates over time constitutes the ensemble of the system. By decomposing this ensemble into independent coupling modes, referred to as eigen microstates, we obtained a set of fundamental spatiotemporal coupling relationships that characterize the behaviour of the system.

Each eigen microstate exhibits distinct features and dynamics and the full system can be reconstructed as a linear superposition of a finite number of these eigen microstates. Notably, the probability distribution of the eigen microstates resembles the Boltzmann distribution found in equilibrium statistical physics. This distribution can be further used to quantify the disorder within the system. The approach enables the identification of critical behaviours and phase transitions, offering a powerful approach for understanding the underlying mechanisms governing complex systems.

The climate system, by nature, operates as a non-equilibrium complex system, often characterized by unknown order parameters and probability density functions. In this study, we treat the SSS in the China Seas as a complex system. Over a temporal span of $M = 254$ months, the temporal average SSS for each grid $i$ ($i = 1,\ldots, N$) was calculated as:

$$\langle \mathrm{SSS}_i \rangle = \frac{1}{M}\sum_{t=1}^{M} \mathrm{SSS}_i(t) \tag{1}$$

Then we calculated the fluctuation of SSS:

$$\widehat{SSS}_i(t) = \mathrm{SSS}_i(t) - \langle \mathrm{SSS}_i \rangle \tag{2}$$

Given the spatial heterogeneity, normalized fluctuations prove advantageous in identifying potential climate modes. The standard deviation was computed as:

$$\Delta_i^{\mathrm{SSS}} = \sqrt{\frac{1}{M}\sum_{t=1}^{M}\left(\widehat{\mathrm{SSS}_i}(t)\right)^2} \tag{3}$$

The state of grid $i$ was normalized as:

$$\delta \mathrm{SSS}_i(t) = \frac{\widehat{\mathrm{SSS}_i}(t)}{\Delta_i^{\mathrm{SSS}}} = \frac{\mathrm{SSS}_i(t) - \langle \mathrm{SSS}_i \rangle}{\Delta_i^{\mathrm{SSS}}} \tag{4}$$

At a given time point $t$, the microstate of the system $\delta\mathrm{SSS}(t)$ can be represented as:

$$\delta \mathrm{SSS}(t) = \begin{bmatrix} \delta \mathrm{SSS}_1(t) \\ \delta \mathrm{SSS}_2(t) \\ \vdots \\ \delta \mathrm{SSS}_N(t) \end{bmatrix} \tag{5}$$

Taking all states into consideration, the SSS complex system can be denoted as $A$, each element of which can be defined as:

$$A_{it}^{\mathrm{SSS}} = \frac{\delta \mathrm{SSS}_i(t)}{C_0^{\mathrm{SSS}}} \tag{6}$$

where $C_0^{\mathrm{SSS}} = M \times N$. By using singular value decomposition, the ensemble matrix can be factorized as:

$$A = U\Sigma V^T \tag{7}$$

which is an $N \times M$ diagonal matrix with elements:

$$\Sigma_{IJ} = \begin{cases} \sigma_I, & I = J \le r \\ 0, & \text{for others} \end{cases} \tag{8}$$

where $r = \min(N, M)$ and $U$ and $V$ are the obtained eigen microstates and their evolution with time.

## Species-distribution model

**Biotic data.** At the outset, we obtained a detailed list of 53 fish species identified for their commercial fisheries from the Food and Agriculture Organization (FAO) Fishery and Aquaculture Statistics database[17] in FAO fishing area 61 that covers our study area.

To develop the habitat suitability model, we compiled a comprehensive database by integrating occurrence records for all 53 species. These records were sourced from two open-access repositories: the Ocean Biogeographic Information System (http://www.iobis.org/) and the Global Biodiversity Information Facility (http://www.gbif.org/). We standardized the taxonomic names of the species using the World Register of Marine Species to ensure consistency. Species with fewer than six occurrence records were excluded, following the approach of ref. 56. This refinement resulted in 31 commercially viable fish species being selected for further analysis.

Systematic measures were implemented to remove duplicate records across databases and entries lacking crucial geographic

information. Additionally, duplicate records within the same grid cell were carefully excluded from further analysis. The final database of species occurrence and location consisted of presence-only points. The number of observed locations for all species considered in this study is presented in Supplementary Table 10.

**Projection of suitable habitats for fish species under current and El Niño marine environments.** We modelled the habitat suitability by MAXNET model[57] implemented on R platform using the Biomod2 package[58]. The hyperparameters of models were tuned individually according to dataset inputs to improve model performance using a built-in method provided by the modelling software. Each model for each cultivated species was generated individually, using five cross-validated iterative runs of four partitions with a maximum of 1,000 pseudo absence background points randomly sampled from a predefined 4-km buffer area around the occurrence point for each species. Thus, 20 runs for each of the four algorithms were generated and then combined using a consensus ensemble approach of each algorithm for each model. Each run of models was then projected onto current and future marine environments independently to estimate a suitability index or fish habitat suitability on each pixel of species. The results of the species-distribution model were validated on the basis of area under the curve method[59]. The final result was obtained by averaging all individual model results on the basis of the criteria of the area under the curve value >0.5. See details of the model settings and validation for the 31 species at https://github.com/Elricriven/Salinity-in-China-Seas.

**Suitability-weighted latitudinal and longitudinal centroids of habitats of species.** To identify a general trend of the spatial changes in the suitable habitats of species, we defined latitudinal and longitudinal centroid of habitat for each stock under non-El Niño and El Niño (considering only salinity-related parameter variations during El Niño years) marine environments modified from ref. 60

$$\mathrm{Lat}C_s = \frac{\sum_{x=1}^{n} \mathrm{Lat}_x \mathrm{SI}_x}{\sum_{x=1}^{n} \mathrm{SI}_x} \tag{9}$$

$$\mathrm{Lon}C_s = \frac{\sum_{x=1}^{n} \mathrm{Lon}_x \mathrm{SI}_x}{\sum_{x=1}^{n} \mathrm{SI}_x} \tag{10}$$

where $\mathrm{Lat}_x$, $\mathrm{Lon}_x$ and $\mathrm{SI}_x$ are the latitudinal, longitudinal coordinates and fish species' habitat suitability at the centre of pixel $x$ for fish species $s$, respectively.

### Convergent cross-mapping analysis

Convergent cross-mapping is a nonlinear causality detection method specifically designed for complex systems[61]. It is a non-parametric state–space approach to causal inference from observational time series. It relies on attractor reconstruction (Takens' theorem[61]): if variable $X$ causally influences $Y$ in a deterministic dynamical system, then the delay-embedded manifold reconstructed from $Y$ (denoted $M_Y$) contains information about $X$. This approach tests this theorem by cross-mapping $X$ and quantifying predictive skill—typically the Pearson correlation between observed $X$ and its cross-mapped estimate ($\hat{X}$). A hallmark of true causation is that this skill increases and then saturates as the library size (the number of points used from $M_Y$) grows, which means that it converges. To assess whether the observed convergence is statistically robust, we performed permutation tests at each library size, in which the driver time series was randomly shuffled while preserving the target. This procedure generates a null distribution of cross-map skill ($\rho$) values against which the observed $\rho$ can be compared. For each library size, a $P$ value was computed as the probability of permuted $\rho$ values greater than or equal to the observed one. A significant causal signal can be identified when (1) $\rho$ increases monotonically with library size, indicating convergence and (2) the observed $\rho$ at the largest library size is significantly higher than the surrogate distribution (typically $P < 0.05$). The dual criteria ensure that we distinguish the genuine causal influence from spurious correlations driven by autocorrelation or shared variability.

## Data availability

The data supporting the findings of this study are available via Science Data Bank at https://www.scidb.cn/en/s/fia6Jv(ref. 62). In situ observational salinity data source can be found in Supplementary Information Section 1. The ocean current data in and around the China Seas are available at https://data.marine.copernicus.eu/. The geopotential height data, 10-m wind speed data and precipitation data are available at https://www.psl.noaa.gov/data/gridded/data.ncep.reanalysis2.html. The river discharge data are available at https://ewds.climate.copernicus.eu/datasets/cems-glofas-historical?tab=download. The Niño 3.4 index data are available at https://psl.noaa.gov/data/correlation/nina34.anom.data. China Fisheries Yearbooks can be downloaded from https://www.zgtjnj.org/. The CMIP6 model data are available at https://esgf-node.llnl.gov/projects/cmip6. FAO data can be found at https://data.fao.org/. Source data are provided with this paper.

## References


53. Sun, Y. et al. Eigen microstates and their evolutions in complex systems. *Commun. Theor. Phys.* **73**, 065603 (2021).
54. Chen, Y. et al. Seasonal predictability of the dominant surface ozone pattern over China linked to sea surface temperature. *npj Clim. Atmos. Sci.* **7**, 17 (2024).
55. Ma, X. et al. Increased predictability of extreme El Niño from decadal interbasin interaction. *Geophys. Res. Lett.* **51**, e2024GL110943 (2024).
56. Van Proosdij, A. S. J., Sosef, M. S. M., Wieringa, J. J. & Raes, N. Minimum required number of specimen records to develop accurate species distribution models. *Ecography* **39**, 542–552 (2016).
57. Renner, I. W. & Warton, D. I. Equivalence of MAXENT and Poisson point process models for species distribution modeling in ecology. *Biometrics* **69**, 274–281 (2013).
58. R Core Team. *R: A Language and Environment for Statistical Computing* (R Foundation for Statistical Computing, 2025).
59. Fawcett, T. An introduction to ROC analysis. *Pattern Recog. Lett.* **27**, 861–874 (2006).
60. Cheung, W. W. L., Brodeur, R. D., Okey, T. A. & Pauly, D. Projecting future changes in distributions of pelagic fish species of Northeast Pacific shelf seas. *Prog. Oceanogr.* **130**, 19–31 (2015).
61. Sugihara, G. et al. Detecting causality in complex ecosystems. *Science* **338**, 496–500 (2012).
62. Wang, Z. et al. Dataset for "ENSO shapes salinity regimes and fish migration in the China Seas". *Science Data Bank* https://cstr.cn/31253.11.sciencedb.34700.CSTR:31253.11.sciencedb.34700 (2026).


## Acknowledgements

We thank L. Guo, Y. Li, Y. Xu, L. Wang, T. Huang, Y. Xu, C. Du, Q. Li and B. Chen for their assistance in sampling and/or analyses. This study was funded by the National Natural Science Foundation of China (grant no. 42188102 to M.D., grant no. 42141001 to X.G., G.W. and Z.W., grant no. 42450183 to J.F., grant no. 12275020 to J.F., grant no. 12135003 to X.C., grant no. 12205025 to J.F. and grant no. 42461144209 to J.F. and X.C.) and partially supported by a grant from the Research Grants Council of the Hong Kong Special Administrative Region, China (grant no. AoE/P-601/23-N to M.D., Z.W. and G.W.) and the Cooperation Project of Zhangzhou Meteorological Bureau (grant no. ZL202402 to Z.W.). J.F. acknowledges support from the Fundamental Research Funds for the Central Universities. X.C. acknowledges support from the National Key R&D Program of China (grant no. 2023YFE0109000).

## Author contributions

All authors contributed to writing and revision of the draft paper. Conceptualization: G.W. and M.D. Data collection: Z.W., H.H., Y.L., X.G. and J.H. Data analysis: Z.W., H.H., T.Q., Y.L., S.L., J.F., J.G., L.C. and X.C. Writing, reviewing and editing: Z.W., G.W. and M.D.

## Competing interests

The authors declare no competing interests.

## Additional information

**Extended data** is available for this paper at https://doi.org/10.1038/s41558-026-02559-3.

**Supplementary information** The online version contains supplementary material available at https://doi.org/10.1038/s41558-026-02559-3.

**Correspondence and requests for materials** should be addressed to Guizhi Wang or Minhan Dai.

**Peer review information** *Nature Climate Change* thanks Kui Zhang and the other, anonymous, reviewer(s) for their contribution to the peer review of this work.

https://doi.org/10.1038/s41558-026-02559-3

**Extended Data Table 1 | The Pearson correlation coefficients and *p* values for variables in Fig. 2**

| X | Y | Pearson correlation coefficient | *p* value |
|---|---|---|---|
| PC1 | E − P | 0.60 | 0.004 |
| PC2 | River discharge | 0.49 | 0.025 |
| PC3 | KCS+KCE | 0.43 | 0.050 |
| Niño index | PC1 | 0.48 | 0.029 |
| Niño index | E − P | 0.55 | 0.010 |
| Niño index | PC2 | 0.68 | 0.001 |
| Niño index | River discharge | 0.55 | 0.010 |
| Niño index | PC3 | 0.73 | 0.001 |
| Niño index | KCS | 0.59 | 0.004 |
| Niño index | KCE | 0.55 | 0.010 |
| ACCD | PC1 | 0.45 | 0.044 |
| ACCD | PC2 | 0.52 | 0.016 |
| ACCD | PC3 | 0.57 | 0.008 |
| Niño index | ACCD | -0.56 | 0.001 |
| Average SSS | Sum of PCs | 0.96 | 0.001 |
| σ of SSS | Sum of PCs | -0.50 | 0.022 |
| Average low SSS (SSS ≤30) | PC2 | -0.49 | 0.025 |
| Average high SSS (SSS ≥34) | PC3 | 0.70 | 0.001 |

https://doi.org/10.1038/s41558-026-02559-3

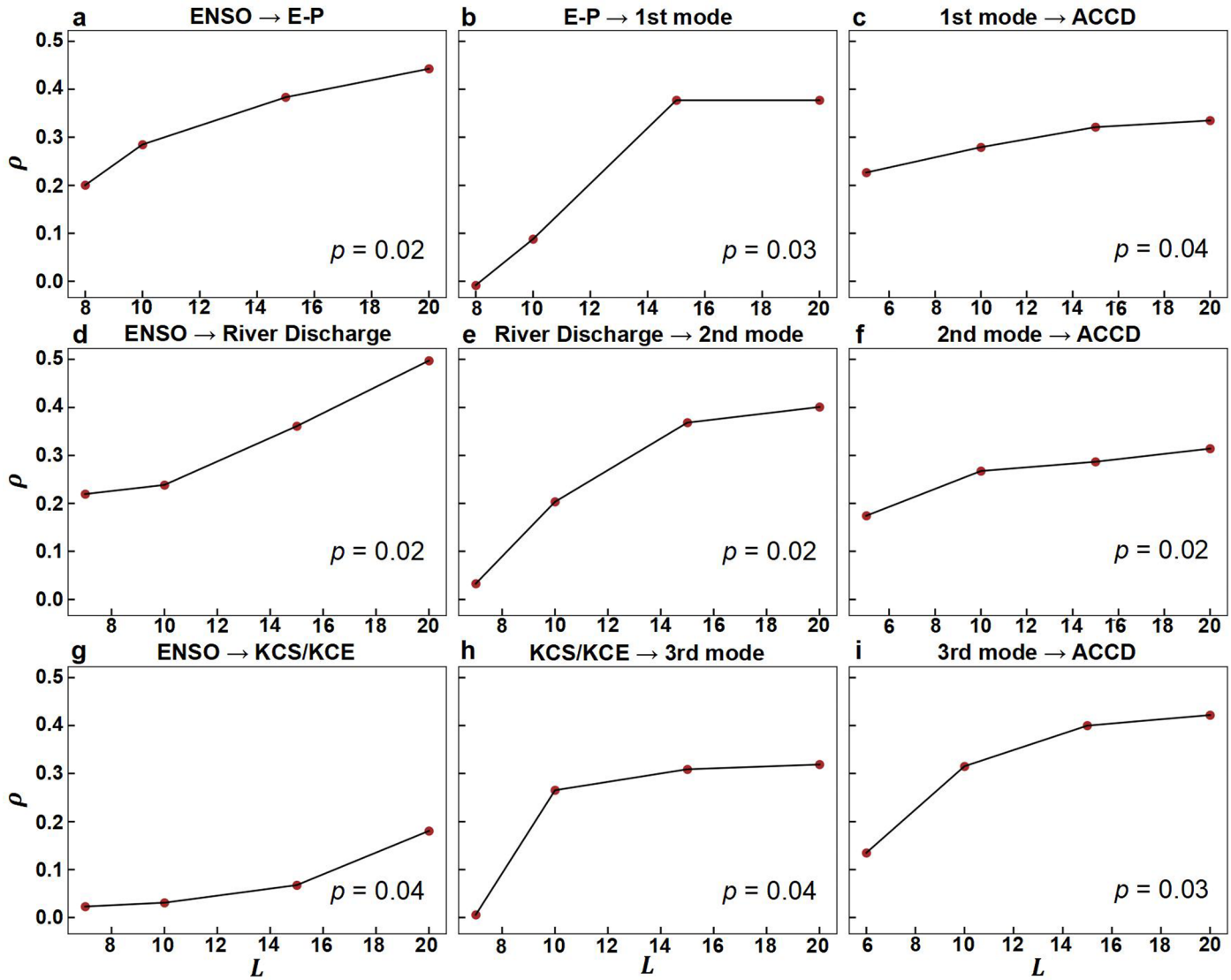


**Extended Data Fig. 1 | Causality of the pathways linking ENSO, SSS variability, and annual change in north-to-south fishery catch differences (ACCD) revealed by Convergent Cross Mapping. a–c**, Causality of the pathway from ENSO to evaporation minus precipitation (E–P) flux to the E–P-dominated SSS mode (the first mode) to ACCD. **d–f**, Causality of the pathway from ENSO to river discharge to the river-dominated SSS mode (the second mode) to ACCD. **g–i**, Causality of the pathway from ENSO to Kuroshio intrusion (KCS/KCE) to the ocean-dominated SSS mode (the third mode) to ACCD. ρ is the skill score of Convergent Cross Mapping, which convergence indicates causation, and L is the library size. ENSO is represented by the Niño 3.4 index. In all pathways, ρ increases monotonically and converges significantly ($P < 0.05$ based on a two-sided bootstrap test with 50,000 resamples), confirming a coherent and statistically robust causal chain linking ENSO forcing, SSS variability, and fishery catch dynamics.

https://doi.org/10.1038/s41558-026-02559-3

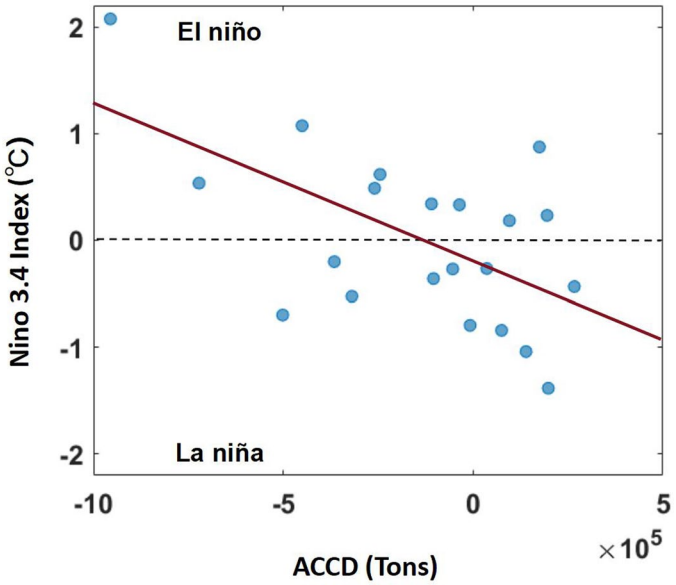


**Extended Data Fig. 2 | Relationship between the Nino 3.4 index and annual change in north-to-south fishery catch differences (ACCD).** $R^2 = 0.32$, n = 21, and $P = 0.007$ based on a two-sided *t*-test.

https://doi.org/10.1038/s41558-026-02559-3

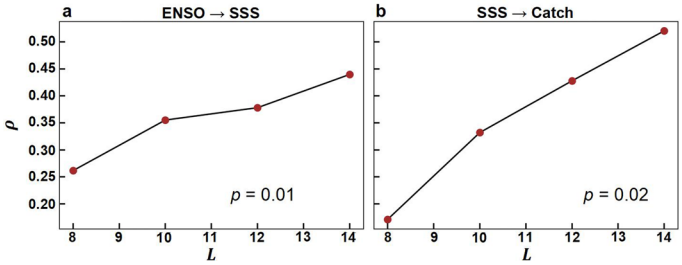


**Extended Data Fig. 3 | Causation pathways between ENSO, SSS, and total fishery catch based on Convergent Cross Mapping. a**, The causality pathway from ENSO to SSS. **b**, The causality pathway from SSS to total fishery catch. ENSO is represented by the Niño 3.4 index. In **a**, **b**, ρ increases monotonically and converges significantly ($P < 0.05$ based on a two-sided bootstrap test with 50,000 resamples), confirming a coherent and statistically robust causal chain linking ENSO forcing, SSS variability and total fishery catch change.

https://doi.org/10.1038/s41558-026-02559-3

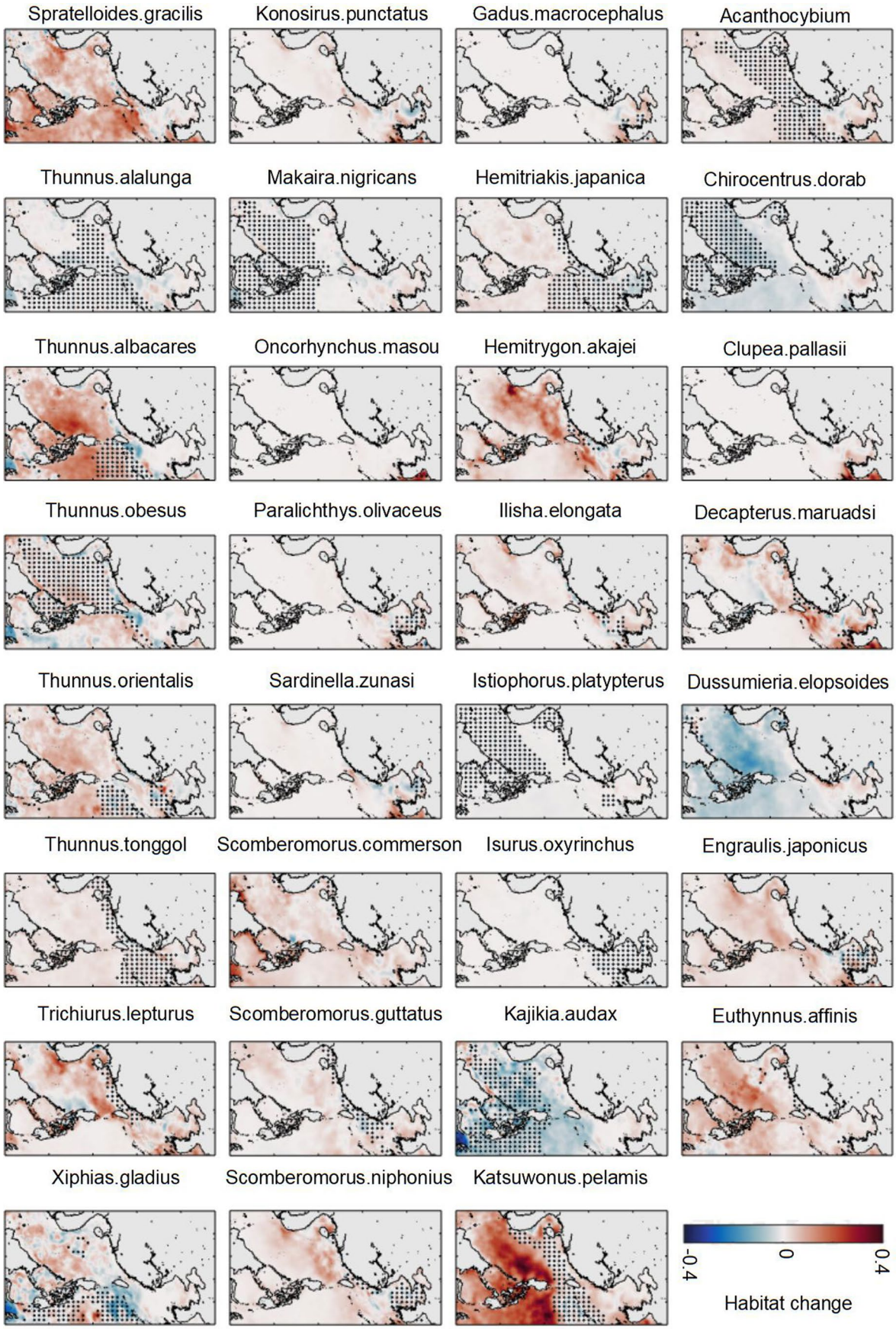


**Extended Data Fig. 4 | Habitat-suitability anomalies for 31 species during El Niño events in the China Seas based on the Species Distribution Model.** Dots stand for the suitable areas under climatological conditions (habitat suitability > 0.5).